Effect of running-in conditions on the super low EHD sliding friction of Si_3N_4 ball and WC plate in glycerol-water solution

Renshui Cao[a], Chenxu Liu[a], Hui Cao[a], Yuanzhe Li[a], Zulfiqar Khan[b], Yonggang Meng[a,*]

[a] *State Key Laboratory of Tribology in Advanced Equipment, Tsinghua University, Beijing 100084, China*

[b] *NanoCorr, Energy & Modelling Research Group, Bournemouth University, Bournemouth, UK*

[*]Corresponding author: mengyg@tsinghua.edu.cn

Abstract: In water-based experiments exploring ultralow or super low friction, the implementation of a running-in period before reaching such states is necessary and important. However, the effect of the change in contact geometry has not been fully realized. In this paper, a series of running-in tests on a Si_3N_4 ball and a WC plate have been performed in glycerol-water mixtures with different concentrations. The shape of the wear scars and the chemical compositions of the worn surfaces were characterized in detail. A numerical EHD and mixed lubrication model was established to comprehensively analyze the effects of geometric profiles, surface roughness, and working / lubrication conditions on ultralow or super low sliding friction. The experiment and simulation results of the study have provided an in-depth understanding of the mechanism of super low friction of liquid lubricated sliding point contacts.

Keywords: running-in, super low friction, contact geometry, silicon nitride, tungsten carbide, glycerol-water

1. Introduction

Water has been known as one of the effective lubricants for engineering ceramics of silicon nitride (Si_3N_4) and silicon carbide (SiC) for more than three decades. In 1987, Tomizawa and Fisher [1] reported the super low sliding friction (coefficient of friction (COF) < 0.002) of self-mated Si_3N_4 and SiC in water, and attributed the super low friction to the tribochemical wear occurred during running-in. Sasaki [2] found that Si_3N_4 and SiC showed super low friction (COF < 0.01) when they slid against a counterpart made of the same material in deionized water, 20-50 times less than that in vacuum, in nitrogen with organic compound vapor or in moist atmosphere, while the

oxides of alumina (Al_2O_3) and zirconia (ZrO_2) did not show super low friction in deionized water. Wong, Umehara and Kato [3] also compared the friction and wear behavior between these four kinds of ceramics mated with themselves in pure water by using a pin-on-disc test rig, and found that all of these ceramics can reach ultralow friction (COF < 0.03) as long as the applied normal pressure is moderate. Chen and Kato [4, 5] compared the running-in behavior between self-mated Si_3N_4 and SiC ball-on-disc pairs in water, and found that Si_3N_4 was superior in achieving a steady-state super low sliding friction (COF < 0.004) with a shorter running-in period comparing with SiC, the steady state COF of which was about 0.01. During the past decade, the families of materials and aqueous lubricants displaying ultralow sliding friction (COF < 0.05) or super low sliding friction (COF < 0.01) have been expanded larger and larger, including the Si_3N_4 ball-on-glass disc and sapphire ball-on-sapphire disc lubricated with phosphoric acid aqueous solution [6], with mixtures of acids and glycerol [7], or with in-situ formed ionic liquids [8], etc. The superlubricity of polyalkylene glycol (PAG) aqueous solutions [9], polyethylene glycol (PEG) aqueous solutions [10], brush-type poly (oligo (ethylene glycol) methyl ether acrylate, P-(OEGMA)) aqueous solution [11], polyhydroxy alcohols [12] and ionic liquids aqueous solution [13] for ceramic materials have been reported. The tribo-material systems which exhibit ultralow or super low sliding friction in aqueous solutions have been extended from ceramics to diamond-like-carbon (DLC) coated contacts [14, 15], tungsten-doped DLC contacts [16], physical vacuum deposition (PVD) TiN coating [17] and even to steel-steel contacts [18].

Among the super lubricious aqueous lubricants mentioned above, the glycerol-water solution is of particular interest. Firstly, glycerol is an odorless, colorless, sweet-taste compound with infinite solubility in water and alcohol [19]. The glycerol-water mixture increases the boiling point of water and decreases the melting point and freeze point substantially, depending on the concentration [20].The friction behavior of glycerol- water mixture also can be changed by controlling the concentration of water [21] or adding [Choline] [Proline] [22]. Secondly, glycerol has been fabricated at a lower cost. It can be synthesized either through reaction processes with fatty acids or

from the propylene from petroleum. In recent years, this chemical has been developed as a co-product of biodiesel production. Thirdly, glycerol-water solutions have been employed widely in a variety of applications, such as cryoprotectants in bioengineering, antifreeze in refrigeration processes and heat transfer fluids for cooling processes. As a good heat transfer fluid, glycerol-water was proved to be the best choice (among glycerol–water, ethylene glycol–water and propylene glycol–water) between the compound parabolic concentrator and the cooling system [23]. From the viewpoint of lubrication, glycerol and glycerol-water mixture are also unique and attractive. Owing to its smaller molecular weight, the viscosity of glycerol increases with pressure much less (pressure-viscosity coefficient ~ 5.0 GPa^{-1}) and decreases with temperature rise much faster than common lubricating paraffin oils and synthesized oils, and its rheological behavior is characterized as an isothermal Newtonian fluid even at very high shear rates [24]. The rheological characteristics of glycerol-water mixtures are between pure glycerol and pure water. That means that glycerol-water mixtures would lead to lower elastohydrodynamic (EHD) friction, although the EHD film thickness would be thinner than the conventional lubricating oils. Therefore, a full film EHD lubrication state with exceptionally low traction can be achieved as long as the surfaces of EHD contacts are smooth enough which would not be possible for common industrial lubricating oils. Besides the benefits of EHD lubrication, glycerol can form ultra lubricious tribofilm (COF ~ 0.02) on hydrogen-free amorphous DLC (a-C) films, firstly reported by Kano [25] in experiments using poly-alpha-olefin (PAO) with 1wt% glycerol mono-oleate (GMO) friction modifier in 2005, and the role played by glycerol in the tribofilm formation has been confirmed later by a few research groups [14, 15, 17, 26]. This implies that not only EHD friction but also boundary friction can be ultralow or even super low, not mentioning the advantages of green and inexpensiveness over the common industrial lubricating oils.

A significant volume of previous experimental findings has been based on either using a ball-on-disc or a pin-on-disc test rig. For the water-based ultralow and super low friction pure sliding experiments observed on a ball-on-disc test rig, all experiments showed a running-in period before achieving the ultralow or super low friction. This is

a feature of the superlubricity of water-lubrication, differing from the structural superlubricity found in monocrystalline MoS_2 [27], graphite [28], graphene [29] and other 2D materials [30] as well as that dominated by hydration lubrication [31]. A considerable number of researchers have noticed the role of the necessary running-in period for achieving water-based superlubricity. Chen and Kato [4] described the running-in of self-mated Si_3N_4 and SiC in water as a slow wear process caused by the tribochemical reactions between water and the ceramic rubbing surfaces, slowly and gradually reducing the surface roughness and resulting in smooth surfaces with roughness Ra~ a few nanometers. They attributed the faster running-in of the Si_3N_4 than the SiC to the narrower energy gap between Si_3N_4 and water (~3 eV) than that between SiC and water (~5.2 eV). According to polyelectronic perturbation theory, the narrower the energy gap the higher the reaction rate. The tribochemically polished smooth wear scar on the ball formed in running-in prepares for the subsequent continuous sliding to get into a full fluid film hydrodynamic or elastohydrodynamic lubrication regime, at which sliding friction can be lower than that of conventional oil lubrication for the sake of the lower pressure-viscosity coefficient and lower viscosity of water-based lubricants than lubricating oils. This standpoint was accepted and used to explain the superlubricity of phosphoric and sulphuric acids where the existence of a high concentration of H^+ ions promotes the tribochemical reactions and hence shortens the running-in period [32, 33]. The hypothesis that EHD lubrication predominates water-based superlubricity was verified with EHD lubricant film thickness measurements in 2014 [32]. The measured EHD film thickness was 17 nm at the sliding speed of 0.15 m/s for a Si_3N_4 ball/Sapphire disc lubricated with a phosphoric acid solution, corresponding to a lambda value (central film thickness/combined surface roughness) of about 3. When the sliding speed was down to 0.018 m/s, the film thickness was less than 10 nm and the measured COF was greater than 0.01. The lubrication state after running-in was also confirmed as EHD-dominant by plotting the measured COF values vs. bearing number on a Stribeck curve [11]. At the mixed lubrication regime, the measured COF was also super low in some cases [33], which was attributed to ultra lubricious tribofilms simultaneously formed on the wear scar

during running-in, as like the tribofilm generated on DLC films [25].

In summary, the effects of running-in on ultralow/super low friction in water-based lubrication have been pointed out as: (1) polishing the initial ceramic surfaces owing to tribochemical wear; (2) transforming the initial concentrated point contact to a less concentrated contact with a slightly crown wear scar on the ball; (3) generating a better boundary film on the rubbing surfaces due to tribochemical reactions at certain appropriate conditions; (4) emission of tiny wear debris that might affect subsequent lubrication. However, another important effect that has not yet come to fruition is the change in contact geometry. In fact, after running-in, the ball/disc contact becomes a non-point contact which is neither the pre-running-in initial ball/disc contact (Fig.1①) nor the post-running-in crown spheric body/disc contact (Fig.1②). The real contact geometry is a combined form of initial spheric shape with a non-spherical slightly crowned surface, as illustrated in Fig.1③-④. Unfortunately, the EHD analysis done previously in references [32] and [34] assumed the point contact after running-in as a ball with a radius equivalent to the curvature of the crown wear scar on a flat disc (Fig.1②). This simplification would lead to inaccurate calculation of the EHD film thickness, because of the deviation of contact geometry from the real one.

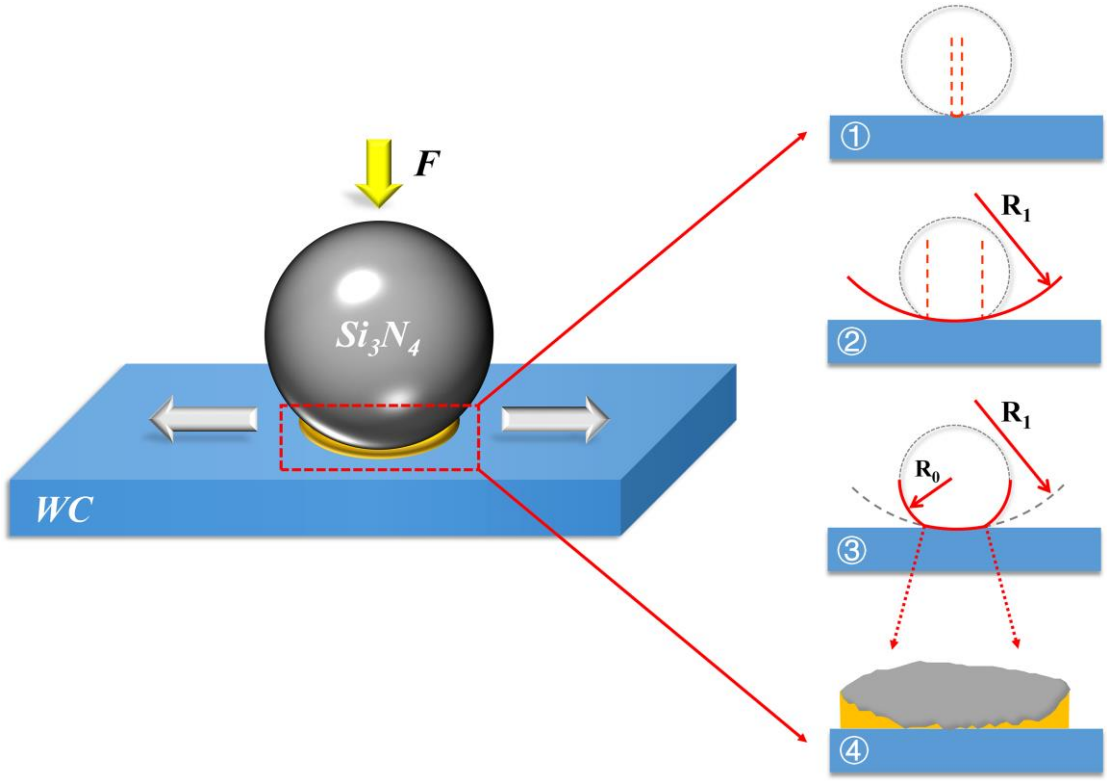

Fig.1 Illustration of the change in contact geometry before and after running-in: ① Initial point contact at pre-running-in; ② Assumed crown spheric body/disc contact at post-running-in; ③ A combined form of initial spheric shape with a crown spheric; and ④ Realistic non-point contact at post-running-in.

In this study, a series of running-in tests on a Si_3N_4 ball and WC plate have been conducted in glycerol-water mixtures with different concentrations under the same load and sliding speed condition in the first stage. In this way, post-running-in ball samples have been observed of assorted sizes of wear scars. In the second stage, reciprocating tests with the different post-running-in Si_3N_4 ball samples were conducted with a fixed glycerol concentration under the same load and reciprocating frequency conditions. And the shape of the wear scars and the chemical compositions of the worn surfaces have been characterised in detail. Numerical EHD and mixed lubrication analyses were conducted to compare the film thickness, elastohydrodynamic pressure, asperity contact pressure, and friction with four different contact geometries (Fig.1 ①–④). The effect of geometry and surface roughness changes of ball samples occurred in running-in on ultralow/super low sliding friction is discussed. The measured and calculated sliding COF is plotted on a Stribeck curve to reveal its transition of lubrication regimes along with the bearing number.

2. Experimental Details and Mathematic Models

2.1. Experimental Details

All friction experiments were conducted on a ball-on-disc apparatus using a Universal Micro-Tribometer (UMT-3, Bruker). The friction pairs are composed of a fixed Si_3N_4 ball (named as upper friction pair) and a reciprocating WC plate (named as lower friction pair, SEEN1203AFTNCR-14 NS740, TUNGALOY MEMBER IMC GROUP). Except for the Stribeck curve test, the remaining experiments have been conducted at the fixed reciprocating frequency of 4 Hz, stroke of 4 mm, and load of 3 N.

The lubricants used in the experiments were pure water (deionized water with resistivity of 18.2 MΩ·cm) and glycerol-water mixtures with different concentrations. The viscosities of different concentrations of glycerol-water mixtures (GLY) under ambient temperature (as shown in Table 1) have been measured in a Cone plate (CP50-1) rheometer with a gap of 0.103 mm.

Table 1 The viscosities of glycerol-water mixtures with different concentrations under ambient temperature 25 °C

Concentrations	Viscosities (mPa·s)
0 % GLY	0.893
20 % GLY	1.545
35 % GLY	2.621
50 % GLY	5.055
65 % GLY	12.266
80 % GLY	42.978
100 % GLY	823.334

The whole running-in tests included two stages. In the pre-running-in stage (20 min), a series of tests on a Si_3N_4 ball and a WC plate have been conducted in glycerol-water mixtures with different concentrations (pure water, 20% GLY, 35% GLY) under the conditions of load 3 N, reciprocating frequency 4 Hz, and stroke 4 mm. In the post-running-in stage (15 min), the contact pairs were still in their original positions, and only lubricants were changed to 80% GLY. After the friction test, friction pairs were conditioned with pure water and ethanol, respectively, and then dried with air-laid papers. A ZYGO-NexView was employed to analyze the surface roughness and obtain realistic non-point contact profiles of wear scars and wear tracks in the form of xyz coordinates. A scanning electron microscope (SEM, FEI Quanta 200 FEG, USA) combined with an energy-dispersive spectroscopy (EDS) was employed to analyze the chemical compositions of the inside and outside areas of the worn surfaces. An X-ray photoelectron spectroscopy (XPS, MFP-3D-SA, USA) was utilized to analyze the chemical composition of the wear scars of the upper friction pairs.

2.2. Mathematic Models

To compare the EHD and mixed lubrication results with different contact geometries, a mixed lubrication model has been established to calculate the pressure, lubricant film thickness, and coefficient of friction within ball-on-disc contacts.

2.2.1. Reynolds Equation

Based on the famous work of Patir and Cheng [35, 36], the average flow Reynolds equation considering the effect of surface roughness is provided in the below equation as:

$$\frac{\partial}{\partial x}(\Phi_x \frac{\rho h^3}{12\eta}\frac{\partial p_h}{\partial x}) + \frac{\partial}{\partial y}(\Phi_y \frac{\rho h^3}{12\eta}\frac{\partial p_h}{\partial y}) = u_s \frac{\partial(\rho h)}{\partial x} + \frac{u_s s}{2} R_q \frac{\partial(\rho \Phi_s)}{\partial x} \quad (1)$$

where Φ_x and Φ_y are the flow factors, ρ and η are the density and the dynamic viscosity of the lubricant respectively, h is the nominal film thickness, p_h is the elastohydrodynamic pressure, u_s is the entrainment sliding velocity and equals to $(u_1+u_2)/2$, s is the slide-roll ratio and equals to $2*(u_1-u_2)/(u_1+u_2)$, R_q is the composite standard deviation of roughness and Φ_s is the shear flow factor.

2.2.2. Asperity Contact Model

As the Si_3N_4 ball slides reciprocally on the WC plate, surface asperity contact might occur frequently under the mixed lubrication. Therefore, the asperity contact pressure must be taken into consideration. In the statistic rough surface contact models, the stochastic rough surface contact model proposed by Kogut and Etsion (KE model) was used in a wide range of applications [37-39]. This model accounts for the elastic, first elastic-plastic, second elastic-plastic, and fully plastic deformation of asperities and it is expressed as follows:

$$p_a = \frac{2}{3}\pi\beta_s K\omega_c^* H_d\left(\int_{d^*}^{d^*+\omega_c^*} I^{1.5} + 1.03\int_{d^*+\omega_c^*}^{d^*+6\omega_c^*} I^{1.425} + 1.4\int_{d^*+6\omega_c^*}^{d^*+110\omega_c^*} I^{1.263} + \frac{3}{K}\int_{d^*+110\omega_c^*}^{\infty} I^{1}\right)$$

$$\begin{cases} I^b = \left(\dfrac{z^* - d^*}{\omega_c^*}\right)^b \Phi^*(z^*)dz^*, \quad K = 0.454 + 0.41\nu_s \\ \omega_c^* = \dfrac{\omega_c}{\sigma_0} = \dfrac{R_{as}}{\sigma_0}\left(\dfrac{\pi K H_d}{E'}\right)^2, \quad d^* = \dfrac{h}{\sigma_0} - \dfrac{1}{\sqrt{48}\pi\beta_s} \\ \dfrac{2}{E'} = \dfrac{1-\nu_s^2}{E_s} + \dfrac{1-\nu_h^2}{E_h} \end{cases} \tag{2}$$

in which β_s is the surface roughness parameter which usually equals 0.05 [40], K is the hardness coefficient of the softer material [41], ω_c^* is the critical interference value of the elastic and the elastoplastic deformation regime, R_{as} is the mean radius of asperity, H_d is the hardness of the softer material, E' is the effective modulus of elasticity, z^* is the asperity height, $\Phi^*(z^*)$ is the asperity heights probability density function assumed to be Gaussian, and d^* is the asperity separation. All the dimensionless values (denoted by *) are normalized by the standard deviation of roughness σ_0.

2.2.3. Film Thickness Equation

The local lubricant film thickness *h* is provided in the below form:

$$h(x,y) = h_0 + g(x,y) + v(x,y) \tag{3}$$

where h_0 is the approach between the two bodies, $g(x,y)$ represents the geometry profile depends on the four types of contact geometry mentioned in Fig.1, and $v(x,y)$ is the sum of elastic deformations of contacting surfaces due to total pressure, calculated by the well-known Boussinesq integration [42]

$$v(x,y) = \frac{2}{\pi E'}\iint_{\Omega}\frac{p_t(x',y')}{\sqrt{(x-x')^2 + (y-y')^2}}dx'dy' \tag{4}$$

in which p_t is the sum of the elastohydrodynamic pressure p_h and the asperity contact pressure p_a.

2.2.4. Thermal effect

The temperature distribution is calculated by the energy equation neglecting the heat conduction in *x*- and *y*- directions and considering the asperity contact, which is written as

$$c\rho(u\frac{\partial T}{\partial x}+v\frac{\partial T}{\partial y}-w\frac{\partial T}{\partial z})=k\frac{\partial^2 T}{\partial z^2}-\frac{T}{\rho}\frac{\partial \rho}{\partial T}(u\frac{\partial p}{\partial x}+v\frac{\partial p}{\partial y})+\eta\left[\left(\frac{\partial u}{\partial z}\right)^2+\left(\frac{\partial v}{\partial z}\right)^2\right]+\tau_a\sqrt{\left(\frac{\partial u}{\partial z}\right)^2+\left(\frac{\partial v}{\partial z}\right)^2} \quad (5)$$

where c and k are the specific heat and conductivity of lubricant respectively, the shear stress of asperity contact τ_a equals to $\mu_a p_a$ and μ_a is the friction coefficient of asperity contact, and *u* and *v* are oil velocities in *x* and *y* directions.

2.2.5 Viscosity equation

The lubricant viscosity is related to pressure and temperature, and one of the commonly used viscosity equations is the Roelands law [43]

$$\eta(p_h,T)=\eta_0\exp\left\{(\ln\eta_0+9.67)\left[-1+(1+5.1\times10^{-9}p_h)^Z(\frac{T-138}{T_0-138})^{-S0}\right]\right\} \quad (6)$$

where η_0 is the ambient viscosity of lubricant at 25 °C, *Z* is the viscosity-pressure index, and *S0* is viscosity-temperature index. *Z* was calculated by $\alpha/5.1\times10^{-9}(ln\eta_0+9.67)$ [44] and depending on the simulation conditions in the reference [34] *Z* was set as 0.3 to all results in this paper. *S0* was set as 1.1 to all results in this paper, which is a common value in calculations of TEHL [45-47].

2.2.6 Load balance and friction coefficient calculation

In the mixed lubrication, the applied load acting on the ball-on-disc contact is braced by the elastohydrodynamic pressure p_h and asperity contact pressure p_a together as follows

$$W=\iint_{\Omega}p_h dxdy+\iint_{\Omega}p_a dxdy \quad (7)$$

where W is the applied load, and Ω means the contact region.

The friction coefficient is determined by

$$\mu=\frac{\iint_{\Omega}\tau_h dxdy+\iint_{\Omega}\tau_a dxdy}{W} \quad (8)$$

where τ_h is the integration of shear stresses in the elastohydrodynamic region.

2.2.7 Numerical model validation

The comparison of results between the numerical model and experiments about

the Si_3N_4 ball / WC plate is discussed in the later sections. Other validation was conducted with experiments on Multi-Function Tribometer (MFT-300, Rtec) with a GCr15 ball and a GCr15 plate in a rotating motion. The experimental conditions and material parameters are provided in Table 2. As shown in Fig. 2, the results of the friction coefficient between experiments and calculations are in good agreement.

Table 2 The experimental conditions and material parameters of rotating tests in MFT-300

Parameter	Value	Parameter	Value
Radius of sphere, mm	6.35	Poisson's ratio of GCr15	0.3
Roughness of ball R_q, μm	0.01	Applied load, N	5
Roughness of plate, μm	0.1	Turning radius, mm	23
Hardness of GCr15, GPa	7.5	Rotate speed, rpm	1~640
Elastic modulus of GCr15, GPa	210	Lubricating oil viscosity @ 40 °C, mPa·s	96.6
Effective elastic modulus E', GPa	231		

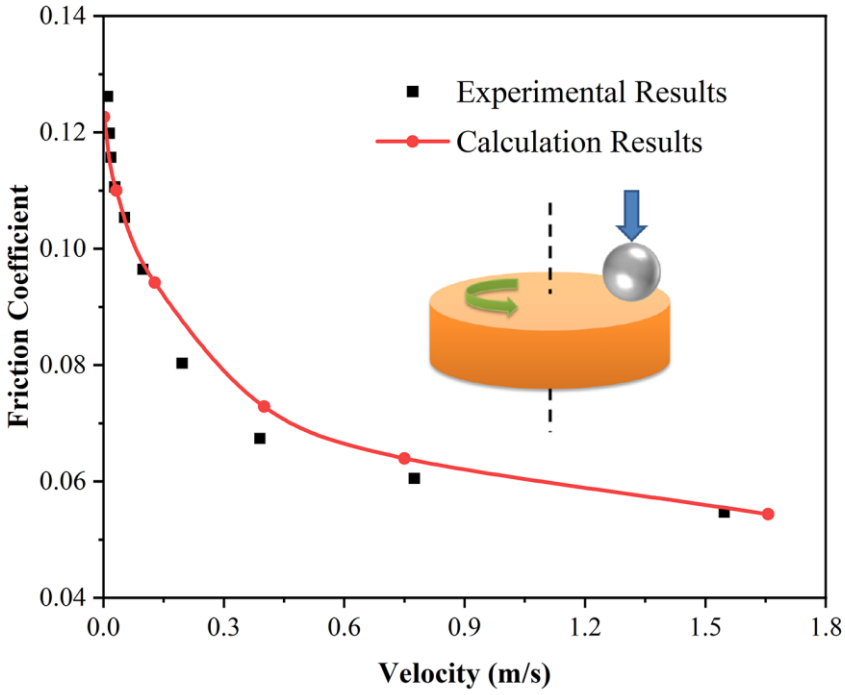

Fig.2 The validation of the numerical model in the MFT-300 rotating tests

3. Results and Discussions

3.1. Experimental results

3.1.1 Pre-running-in stage

The blue lines in Fig.3 show the variation of friction coefficient during the pre-running-in stage. In this stage, the initial point contact gradually transformed into a coronal scar due to the wear of the contact pair. There is no doubt that the pre-running-in stage determined the main profiles of wear scars. Thus, for the 6.35 mm diameter balls, the diameters of coronal scars decreased as the viscosities of lubricants increased (pure water – 20% GLY – 35% GLY), and the highest COF showed in the pure water running-in condition. Under certain conditions, the COFs sharply decreased, due to the good consistency of the meshing of the contact pairs. In addition, when changing to a 3.97 mm diameter ball, the diameter of the wear scar and COF differed from that of a 6.35 mm diameter ball because of changes in the contact pressure and contact profile.

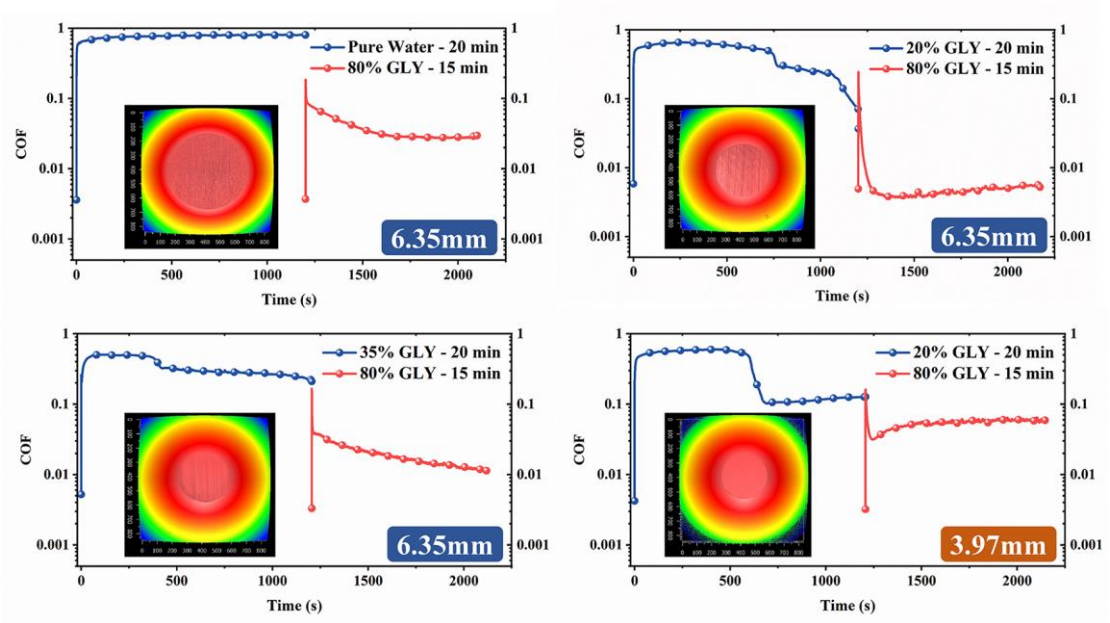

Fig.3 The variation of friction coefficient during the pre-running-in stage and post-running-in stage under the conditions of load 3 N, reciprocating frequency 4 Hz, and stroke 4 mm for a 6.35mm diameter Si_4N_3 ball and a 3.97mm diameter Si_4N_3 ball.

3.1.2 Post-running-in stage

After the pre-running-in stage lubricants were changed to 80% GLY with a viscosity of 42.978 mPa·s. As shown in Fig.3, each COF curve had a peak at the beginning and gradually decreased thereafter. The main reason is that when replacing the lubricants, the surfaces of the contact pairs were conditioned and the conditions for good meshing consistency deteriorated which resulted in the emergence of a new short-term running-in stage. It is interesting to note that the COFs had a huge decrease compared to that in the pre-running stage. The first reason is that the viscosity was higher and the lubrication state was better than the pre-running-in stage. Another reason is that a sizable number of wear particles have been identified in the lubricants after the pre-running-in stage which naturally leads to higher COF. And all of these wear particles were conditioned by changing 80% GLY lubricants.

3.1.3 Comparison of wear scar surfaces

The ZYGO-NexView was employed to analyze the surface roughness of different wear scars after the post-running-in stage. Considering the average flow Reynolds equation used in the calculation, low-pass filtering was performed in the ZYGO-NexView software with different short-period cutoff values (10 μm and 20 μm) to preserve contours without roughness information. Fig.4 indicates that glycerol-water mixtures with different concentrations lead to different surface profiles and surface qualities. It also can be seen that the larger the short-period cutoff value, the smoother the contour. However, all surfaces measured were exceptionally smooth with a few nanometers ($R_q \leq 15$ nm) of surface roughness due to the polishing effect of the running-in stages.

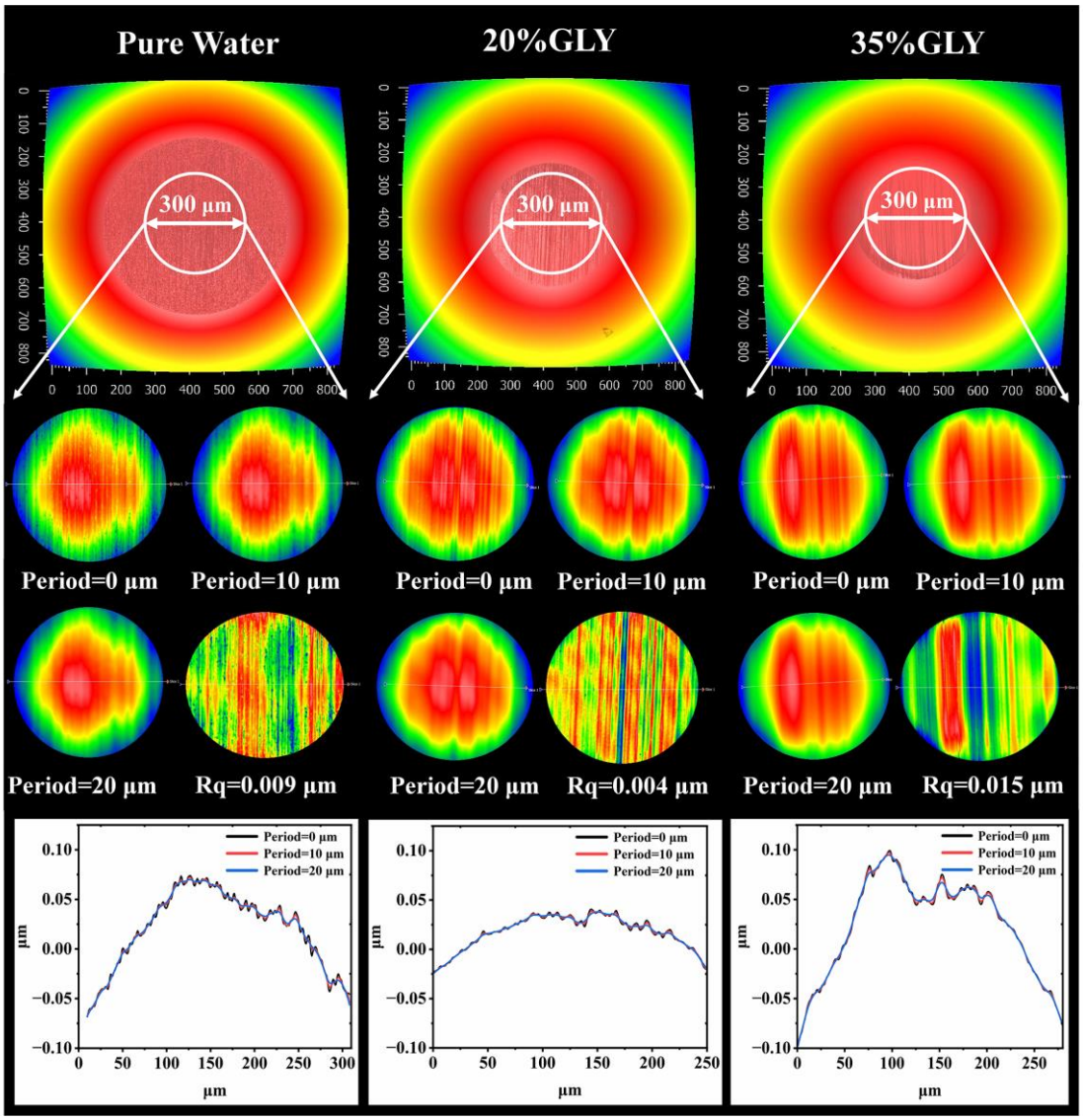

Fig.4 Surface comparison and filtering of wear scars on 6.35 mm diameter balls after the post-running-in stage

3.1.4 The chemical compositions analysis

Fig.5 shows the morphology and chemical composition of the wear track on the lower friction pair after the pre-running-in stage in 20% GLY and the post-running-in stage in 80% GLY. According to the 3D morphology in Fig.5 (a), the depth and width of the wear track are around 0.1 μm and 320 μm, respectively. The microstructures inside and outside areas of the worn surface are the same as shown in the SEM observation in Fig.5 (b). In addition, the EDS results in Fig.5 (c) and Fig.5 (d) show that the elemental composition inside and outside the wear track contains Co, W, Nb, Ti and Ni with a small amount of C and N. O element inside and outside the wear track

was not found to be present. These results indicate that no chemical reaction or tribochemical reaction occurs inside the wear track of the lower friction pair.

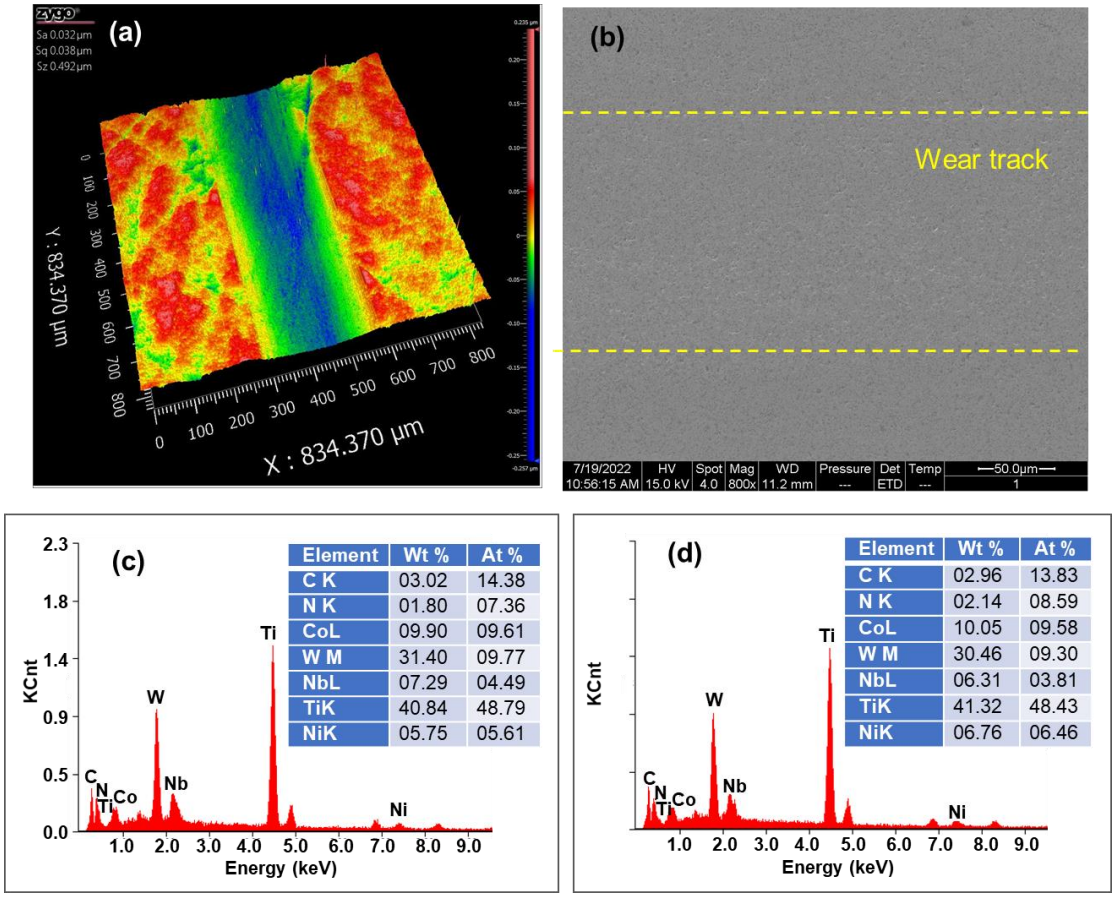

Fig.5 Morphology and chemical composition of the wear track on the lower friction pair after the pre-running-in stage in 20% GLY and the post-running-in stage in 80% GLY: (a) 3D morphology measured by ZYGO-NexView; (b) morphology measured by SEM; (c) and (d) present the EDS elemental compositions of the inside and outside areas of the worn surface, respectively.

Chemical compositions of wear scars on the upper friction pairs were analyzed combining with the XPS results. Here, we chose three upper friction balls to analyze the effect of the chemical compositions of wear scars on the friction forces or COFs.

Fig.6, Fig.7 and Fig.8 present the XPS spectra, recorded from the wear scars obtained after the pre-running-in stage in pure water then the post-running-in stage in 80% GLY with a 6.35 mm diameter ball as the upper friction pair (Fig.6), the pre-running-in stage in 20% GLY and the post-running-in stage in 80% GLY with a 6.35 mm diameter ball as the upper friction pair (Fig.7), and the pre-running-in stage in 20%

GLY and the post-running-in stage in 80% GLY with a 3.97 mm diameter ball as the upper friction pair (Fig.8). According to Fig.3, the COF in the post-running-in stage corresponding to the above three samples are 0.0383, 0.0061 and 0.0535 respectively.

Fig.6, Fig.7 and Fig.8 show C 1s peaks located at around 284.5 eV in which are considered to be the carbon from the environment. In Fig.7 or Fig.8, another C 1s peak located at 286.6 eV is attributed to glycerol. For the case of the pre-running-in stage in 20% GLY, glycerol is adsorbed on the wear scar of the ceramic ball. While, in the case of the pre-running-in stage in pure water, there is no glycerol adsorption. The N 1s peaks located at around 397.2 eV are attributed to Si_3N_4 in Fig.6, Fig.7 and Fig.8. In addition, the two peaks for Si at 101.7 eV and 102.5 eV are due to Si_3N_4 and silicates respectively.

Although the chemical composition of the wear scars in Fig.7 and Fig.8 is similar, their COFs are significantly different. The results indicate that the formation of silicates may cause the friction coefficient to decrease to 0.05. It is not the main factor causing the super low friction. The realization of super low friction requires lower contact pressure.

The W 4f peaks indicate a small amount of transfer substance from the lower friction surface to the upper friction surface. For the case of pre-running-in stage in pure water (Fig.6), under the combined action of high friction and water, a portion of W metal was oxidized into WO_x. For the case of pre-running-in stage in 20% GLY (Fig.7 and Fig.8), the valence state of W element is 0. It indicates the main form of W is metal or alloy.

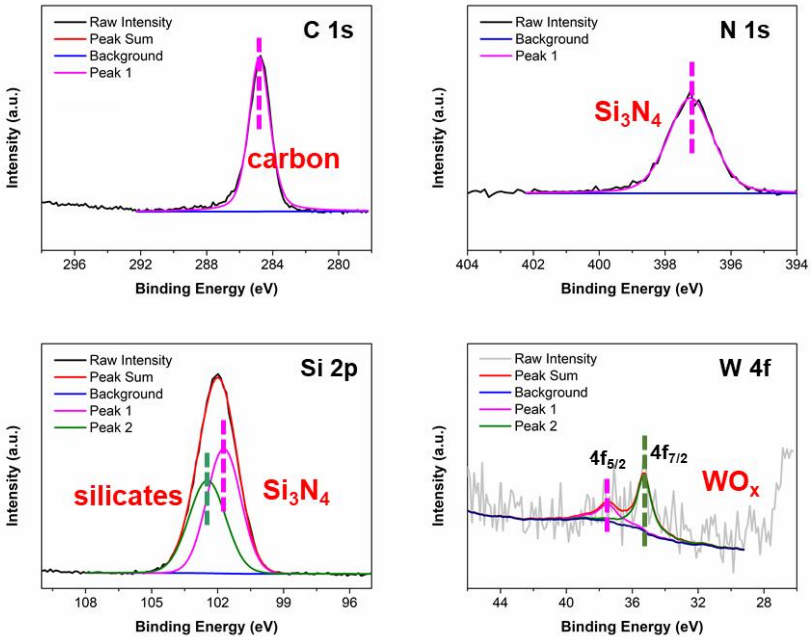

Fig.6 XPS spectra of the C 1s, N 1s, Si 2p and W 4f of the wear scars of the upper friction pairs obtained under the pre-running-in stage in pure water and the post-running-in stage in 80% GLY with a 6.35 mm diameter ball as the upper friction pair.

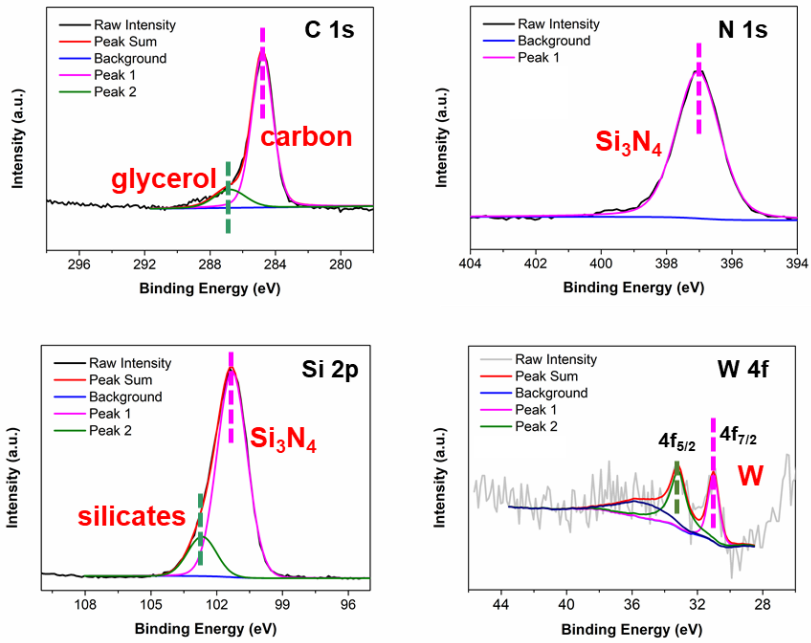

Fig.7 XPS spectra of the C 1s, N 1s, Si 2p and W 4f of the wear scars of the upper friction pairs obtained under the pre-running-in stage in 20% GLY and the post-running-in stage in 80% GLY with a 6.35 mm diameter ball as the upper friction pair.

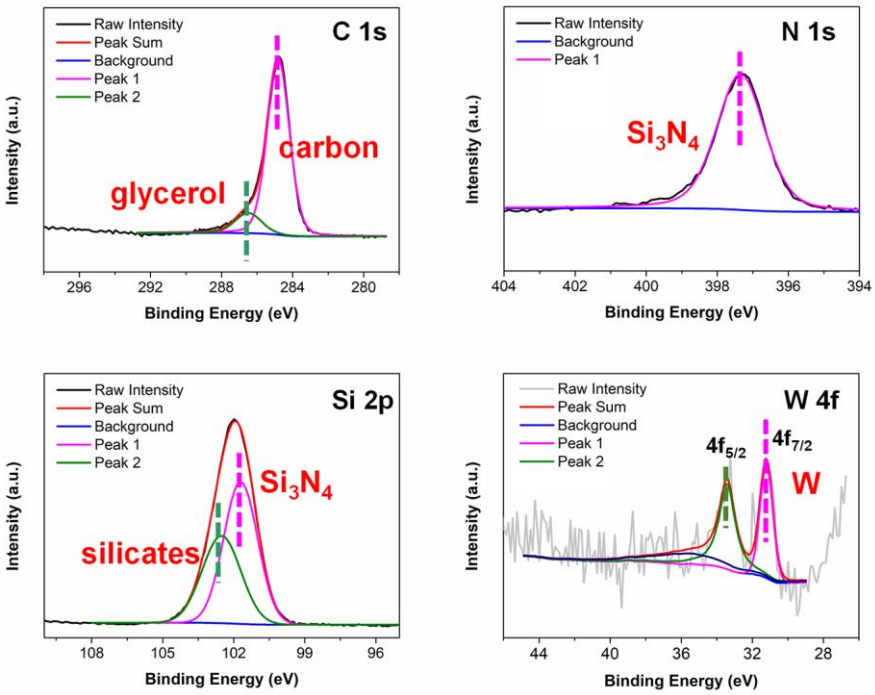

Fig.8 XPS spectra of the C 1s, N 1s, Si 2p and W 4f of the wear scars of the upper friction pairs obtained under the pre-running-in stage in 20% GLY and the post-running-in stage in 80% GLY with a 3.97 mm diameter ball as the upper friction pair.

3.2. Calculation results

The above-mentioned experimental results have attracted us to consider the crucial factors for achieving ultralow or super low sliding friction. Thus, the mixed lubrication model established in Sect.2.2 was employed to study the significance. All the results below are based on experiments with 6.35mm diameter balls and WC plates and the main input parameters of calculation are provided in Table 3.

Table 3 Main input parameters of calculation

Parameter	Value	Parameter	Value
Radius of sphere, R, mm	6.35	Poisson's ratio, $\nu_{s,h}$	0.3
Applied load, W, N	3	Asperity contact friction coefficient, μ_a	0.14
Sliding velocity, u_s, m/s	0.016	Slide-roll ratio, s	2
Ambient viscosity, η_0, mPa·s	42.978	Ambient temperature, T_0, K	298
Effective elastic modulus, E', GPa	332		

3.2.1 Low pass filter processing

In Sect.2.2, the average flow Reynolds equation is employed to calculate the elastohydrodynamic pressure, where Φ_x and Φ_y are the flow factors considering the effect of surface roughness. Therefore, if we want to use realistic non-point contact profiles obtained from ZYGO-NexView to represent $g(x,y)$ in Eq.3, a low pass filter processing is needed. As shown in Fig.4, three types of short periods (0 μm, 10 μm, and 20μm) were chosen to filter the profiles. The results of pressure distributions and film thicknesses with these filter processing profiles based on 20% GLY running-in (including 20% GLY pre-running-in stage and 80% GLY post-running-in stage) origin profile is provided in Fig.9. We can see that the curves are similar, with the only difference being that the larger the brief period is, the smoother the curve. Considering the roughness in nanometres magnitude and the similar results, the 20 μm short period was selected and used in the subsequent calculations.

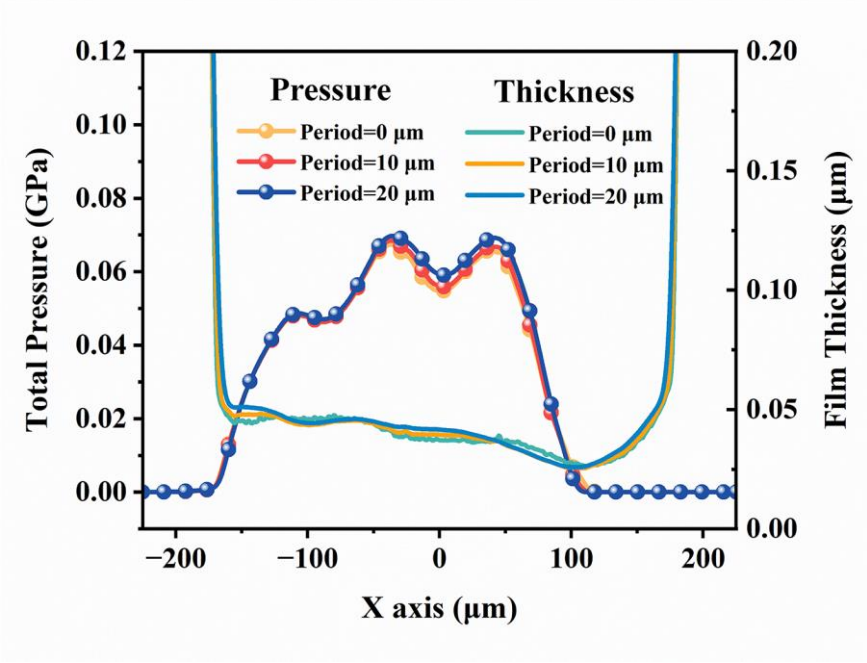

Fig.9 Pressure distributions and film thicknesses with different low pass filter processing profiles based on 20% GLY running-in profile

3.2.2 Comparison of four contact geometries

In Sect.1, four various contact geometries are introduced to explain the transformation of the contact area. Fig.10 and Fig.11 indicate that the

elastohydrodynamic pressure distributions, asperity contact pressure distributions, film thickness, and friction forces with these geometries are hugely different. For the initial point contact at pre-running-in (Fig.10 (a), B=35 μm, R=6.35 mm), due to the smallest contact area, the pressure distributions are highest among the four geometries, which leads to the thinnest film thickness and larger frictional force (Fig.11). Though the assumed crown spheric body/disc contact at post-running-in (Fig.10 (b), B=185 μm, R_1= 467.6 mm) has low elastohydrodynamic pressure and almost zero asperity contact pressure, its geometry is not realistic, which would lead to inaccurate calculation of the EHD film thickness (Fig.11 (a)). When combined with the initial spheric shape and the crown spheric shape (Fig.10 (c), B=185 μm, R_1=467.6 mm, R_0=R=6.35 mm), the elastohydrodynamic pressure is lower than the initial point contact as well. However, the asperity contact pressure near the inlet area is higher, which is the reason for the maximum friction force (Fig.11). Compared with the three geometries discussed, the realistic non-point contact (Fig.10 (d)) has the best performance and amazing super low friction.

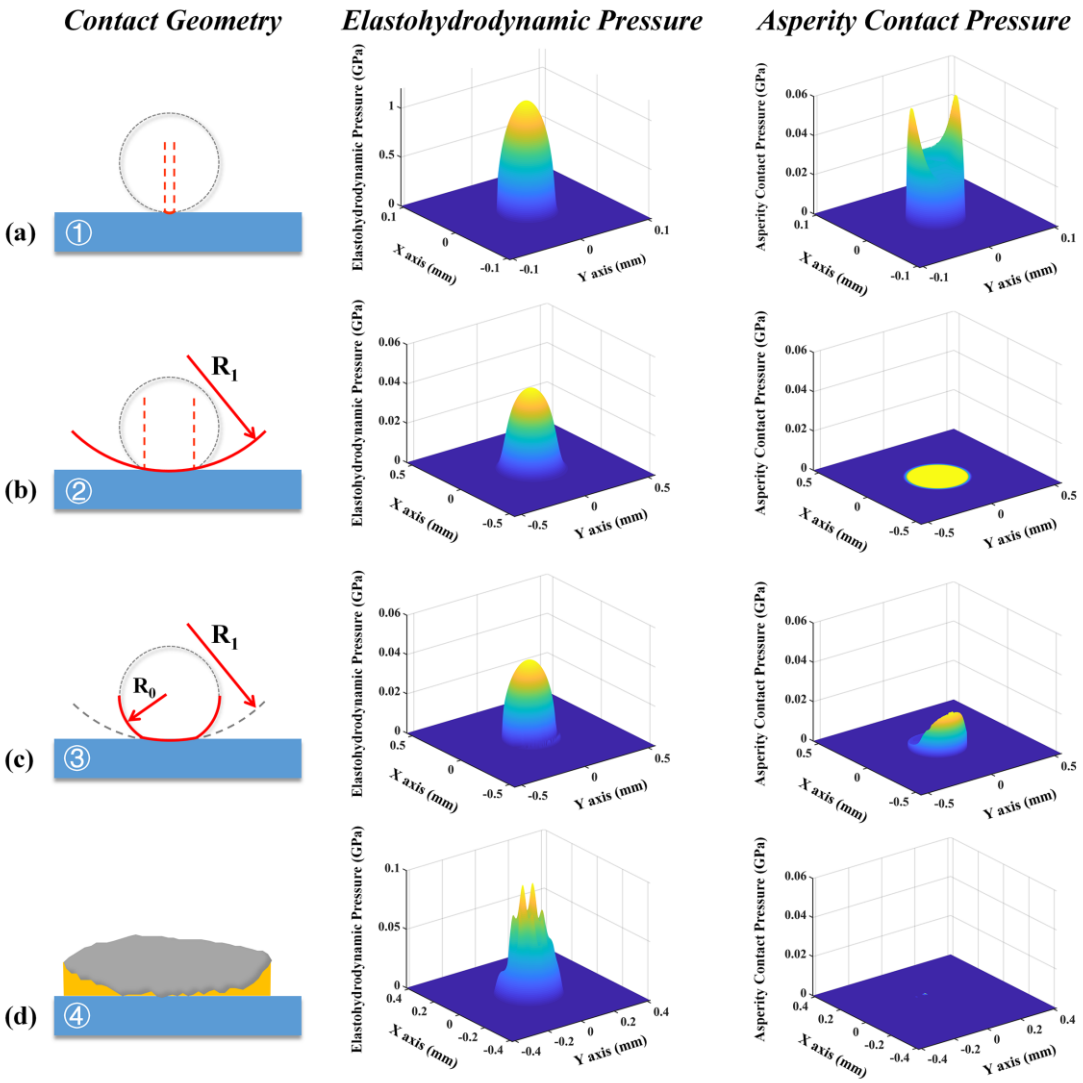

Fig.10 Elastohydrodynamic pressure distributions and asperity contact pressure distributions with different contact geometries based on 20% GLY running-in condition

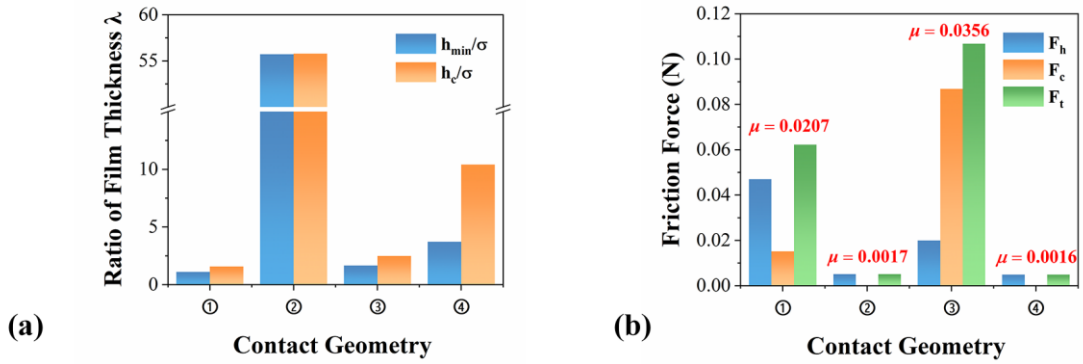

Fig.11 Ratio of film thickness and friction force with different contact geometries based on 20% GLY running-in condition

Because of inputting the same working condition and the same roughness, the

profiles of four geometries have been compared to study the differences between them, as shown in Fig.12. It is clear that near the inlet region, the transition of the combined profile (③) is not smooth, which is the main reason for increasing asperity contact pressure. On the contrary, the realistic non-point contact profile has a wonderful transition that helps more oil get into the contact area and decreases the possibility of asperity contact. Thus, a good profile transition near the inlet region is important to achieve super low friction conditions.

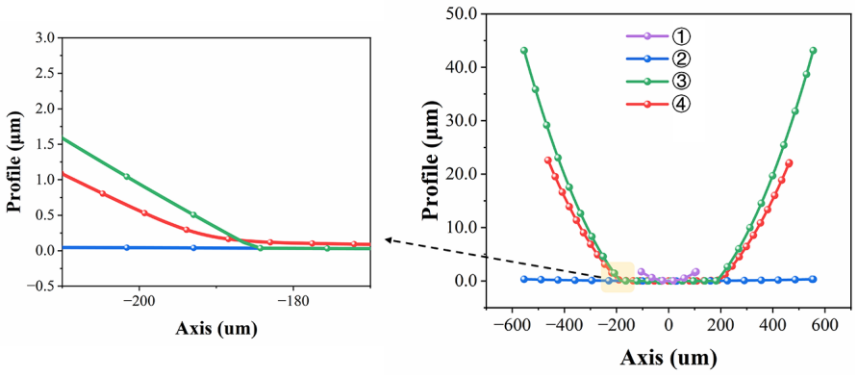

Fig.12 The profile comparisons between four geometries

3.2.3 The contact half-width and rounding radius effects

A series of profiles with different contact half-widths and rounding radii have been included as a smooth transition has a beneficial effect. Fig.13 indicates the variation of friction coefficient versus different contact half-widths and rounding radii. No matter what contact half-width is, no rounding radius profile always has a large COF. When the contact half-width is below 125 μm, only a smaller rounding radius is needed to obtain a lower COF. On the other hand, a larger rounding radius is utilized for wider contact half-width. However, the COF of a wider contact half-width can achieve super low friction conditions, while a narrower half-width is difficult to achieve. Therefore, it is concluded here that a perfect geometry with a suitable contact half-width and an appropriate rounding radius is incredibly significant to achieve super low friction.

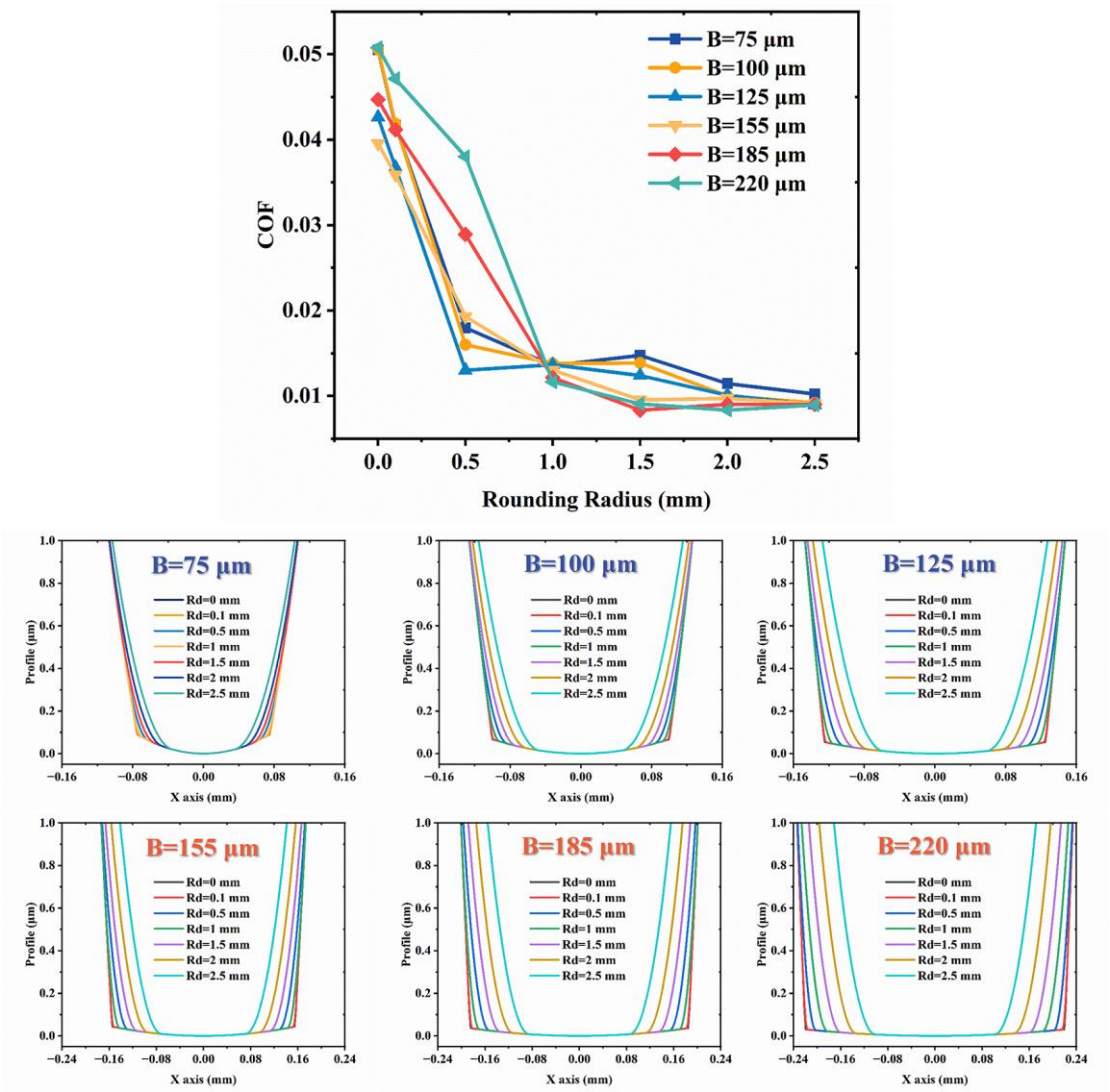

Fig.13 The variation of friction coefficient versus different half-widths and rounding radii

3.2.4 The surface roughness effects

As mentioned in Sect. 3.1.3, the surface roughness after the post-running-in stage is at the nanometer level. The effects of changing surface roughness have been analyzed when the profile and working condition are constant. Due to the film thickness of insignificant number of parts in the contact region being below 10 nm (Fig.14 (d)), a slight increase in surface roughness will cause direct contact with rough peaks (Fig.14 (c)). And that is also the main reason for the low film thickness ratio and high friction force (Fig.14 (a)). Thus, another crucial factor about super low friction has been found after the running-in stage, nanoscale surface roughness is needed to reduce the contact

with rough peaks.

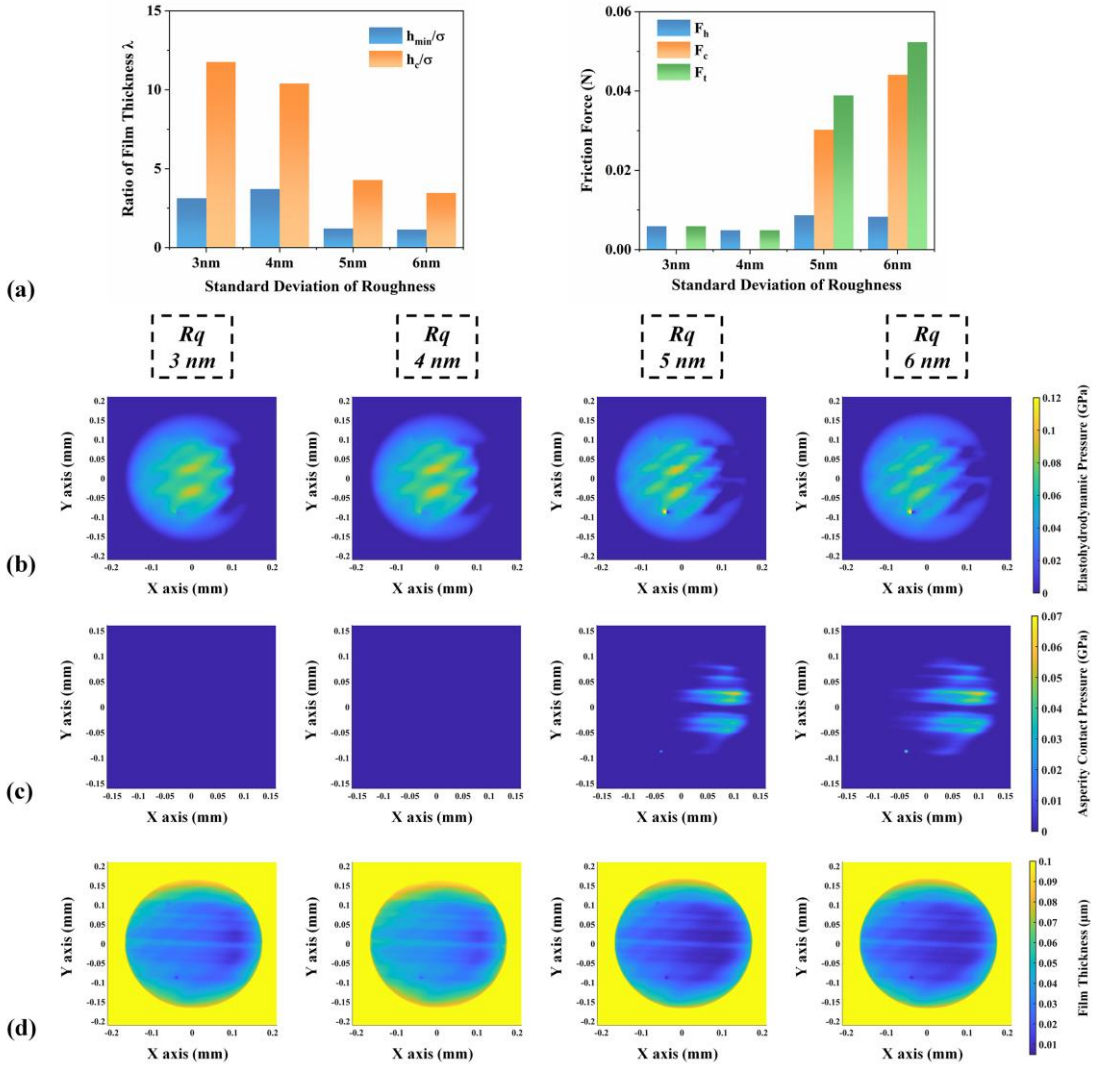

Fig.14 The effect of roughness on (a) ratio of film thickness and friction force; (b) elastohydrodynamic pressure distribution; (c) asperity contact pressure distribution; and (d) film thickness distribution

3.2.5 Effects of working/lubrication conditions

As shown in Fig.15, the measured and calculated sliding COF is plotted on a Stribeck curve to reveal its transition of lubrication regimes along with the bearing number. For the experimental part, after the pre-running-in stage under the working condition of 20% GLY, 3 N, 4 Hz, 4 mm, and 20min, the lubricants were changed to 80% GLY and a series of post-running-in experiments under different loads (0.5 N, 1 N, 3 N) and frequencies (0.2 Hz, 0.5 Hz, 1 Hz, 2 Hz, 4 Hz) were conducted. For the

calculation part, the realistic non-point contact profiles and the values of roughness obtained from the ZYGO-NexView were deployed in calculating. We can see that the tendencies of experimental results and calculation results accord with each other. The differences between them are because of several reasons: First, the friction coefficient of asperity contacts μ_a in the calculations was set as 0.14, which means even asperity peaks bear all the applied load, the COF can only achieved at 0.14. Second, there is no doubt the profiles and surface roughness are different under different working conditions. However, in the calculation, profiles and surface roughness have been assumed to be constant for the working conditions. In this way, it also means that even if the profiles have a suitable contact half-width and an appropriate rounding radius, and the nanoscale surface roughness has been achieved, super low friction will never be achieved without good working conditions. And the best working condition is in the transition region between the mixed lubrication and EHD, which corresponds to the lowest turning point on the Stribeck curve.

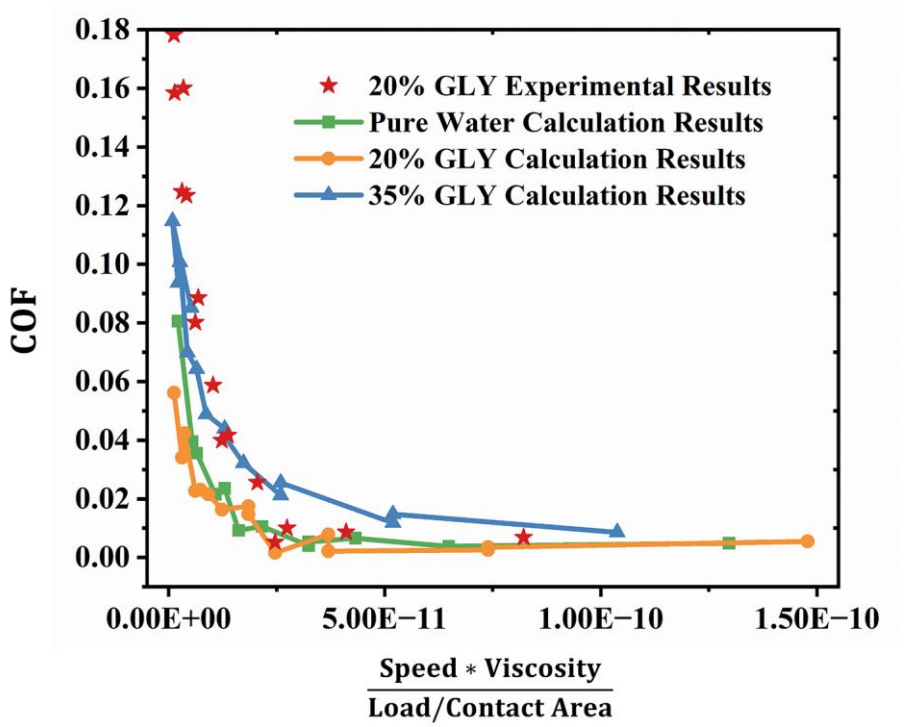

Fig.15 The effect of working/lubrication conditions through Stribeck curve

4. Conclusions

The effects of the running-in conditions on the super low sliding friction of Si_3N_4 ball and WC plate in glycerol-water solution were comprehensively analyzed from the aspects of both experimental and simulation. From the results, there are three key factors that affect the possibility of arriving super low friction. Firstly, during the running-in stage, the geometric profile of the ball should transform the initial concentrated point contact into a less concentrated contact with a slightly crown wear scar, which means a suitable contact half-width and an appropriate rounding radius are both needed. Secondly, nanoscale surface roughness must be achieved to reduce the contact with rough peaks after the running-in stage. Besides, a good working/lubrication condition is significant as well. From the Stribeck curve (Fig.15), there is no doubt that the optimal condition is for the bearing number to be between the transition stage from mixed lubrication to EHD.

Conflicts of interest

There are no conflicts to declare.

Data availability statement

All experimental and simulation data are available if requested.

Acknowledgment

The authors would like to acknowledge both direct and in-kind funding to support this study by the National Natural Science Foundation PR China Grant No. 51635009 and the Global Visiting Fellowship Award No. DDZZCC.X Bournemouth University, United Kingdom.

510 **Nomenclature**

B	Hertzian contact half-width, m	T_0	ambient temperature, K
c	specific heat of lubricant, J/(kg·K)	u, v	oil velocities in x and y directions, m/s
d^*	dimensionless asperity separation	u_s	entrainment sliding velocities, m/s
E'	effective elastic modulus, Pa	$\nu_{s,h}$	Poisson's ratio of softer material and harder material
$E_{s,h}$	elastic modulus of softer material and harder material	$\nu(x,y)$	elastic deformation, m
$g(x,y)$	original geometry profile, m	W	applied load, N
h	nominal film thickness, m	Z	viscosity-pressure index, 0.3
h_0	approach between the two bodies, m	z^*	dimensionless asperity height
H_d	hardness of the softer material, Pa	β_s	surface roughness parameter
k	thermal conductivity of lubricant, W/(m·K)	η	dynamic viscosity of lubricant, Pa·s
K	hardness coefficient, 0.454+0.41 υ	η_0	ambient dynamic viscosity of lubricant, Pa·s
p_a	asperity-contact pressure, Pa	μ_a	coefficient of asperity contact, 0.14
p_h	elastohydrodynamic pressure, Pa	ρ	density of lubricant, kg/m^3
p_t	total pressure, Pa	τ_a	shear stress of asperity contact, Pa
R	Radius of sphere, m	τ_h	shear stress of elastohydrodynamic region, Pa
R_{as}	mean radius of asperity, m	Φ_s	shear flow factor
R_q, σ_0	composite standard deviation of roughness, m	Φ_x, Φ_y	flow factors
Rd	rounding radius, m	ω_c^*	dimensionless critical interference
s	slide-roll ratio, 2*(u_1-u_2)/ (u_1+u_2)	Ω	contact regime
$S0$	viscosity-temperature index, 1.1		

511

512

References

[1] Tomizawa H, Fischer TE. Friction and Wear of Silicon-Nitride and Silicon-Carbide in Water - Hydrodynamic Lubrication at Low Sliding Speed Obtained by Tribochemical Wear. Asle Transactions. 1987;30:41-6.

[2] Sasaki S. The Effects of the Surrounding Atmosphere on the Friction and Wear of Alumina, Zirconia, Silicon-Carbide and Silicon-Nitride. Wear. 1989;134:185-200.

[3] Wong HC, Umehara N, Kato K. Frictional characteristics of ceramics under water-lubricated conditions. Tribology Letters. 1998;5:303-8.

[4] Chen M, Kato K, Adachi K. The difference in running-in period and friction coefficient between self-mated Si3N4 and SiC under water lubrication. Tribology Letters. 2001;11:23-8.

[5] Chen M, Kato K, Adachi K. Friction and wear of self-mated SiC and Si3N4 sliding in water. Wear. 2001;250:246-55.

[6] Li JJ, Zhang CH, Luo JB. Superlubricity Behavior with Phosphoric Acid-Water Network Induced by Rubbing. Langmuir. 2011;27:9413-7.

[7] Li JJ, Zhang CH, Ma LR, Liu YH, Luo JB. Superlubricity Achieved with Mixtures of Acids and Glycerol. Langmuir. 2013;29:271-5.

[8] Ge XY, Li JJ, Zhang CH, Liu YH, Luo JB. Superlubricity and Antiwear Properties of In Situ-Formed Ionic Liquids at Ceramic Interfaces Induced by Tribochemical Reactions. Acs Applied Materials & Interfaces. 2019;11:6568-74.

[9] Wang HD, Liu YH, Li JJ, Luo JB. Investigation of Superlubricity Achieved by Polyalkylene Glycol Aqueous Solutions. Advanced Materials Interfaces. 2016;3.

[10] Ge XY, Li JJ, Zhang CH, Luo JB. Liquid Superlubricity of Polyethylene Glycol Aqueous Solution Achieved with Boric Acid Additive. Langmuir. 2018;34:3578-87.

[11] Jia WP, Bai PP, Zhang WL, Ma LR, Meng YG, Tian Y. On Lubrication States after a Running-In Process in Aqueous Lubrication. Langmuir. 2019;35:15435-43.

[12] Matta C, Joly-Pottuz L, Bouchet MID, Martin JM. Superlubricity and tribochemistry of polyhydric alcohols. Physical Review B. 2008;78.

[13] Espinosa T, Jimenez M, Sanes J, Jimenez AE, Iglesias M, Bermudez MD. Ultra-Low Friction with a Protic Ionic Liquid Boundary Film at the Water-Lubricated Sapphire-Stainless Steel Interface. Tribology Letters. 2014;53:1-9.

[14] Bouchet MID, Matta C, Le-Mogne T, Martin JM, Zhang Q, Goddard WA, et al. Superlubricity mechanism of diamond-like carbon with glycerol. Coupling of experimental and simulation studies. International Conference on Science of Friction. 2007;89.

[15] Bjorling M, Shi YJ. DLC and Glycerol: Superlubricity in Rolling/Sliding Elastohydrodynamic Lubrication. Tribology Letters. 2019;67.

[16] Arshad MS, Kovac J, Cruz S, Kalin M. Physicochemical and tribological characterizations of WDLC coatings and ionic-liquid lubricant additives: Potential candidates for low friction under boundary-lubrication conditions. Tribology International. 2020;151.

[17] Fu XJ, Cao L, Qi CX, Wan Y, Xu CH. Ultralow friction of PVD TiN coating in the presence of glycerol as a green lubricant. Ceramics International. 2020;46:24302-11.

[18] Chen Z, Liu YH, Luo JB. Superlubricity of nanodiamonds glycerol colloidal solution between steel surfaces. Colloids and Surfaces a-Physicochemical and Engineering Aspects. 2016;489:400-6.

[19] Solomons TWG, Fryhle CB. Organic chemistry. 9th ed. Hoboken, N.J: John Wiley distributor; 2007.

[20] Medeiros PSG, Barbosa CRF, Fontes FdAO. Effects of addition glycerol co-product of biodiesel in the thermophysical properties of water-glycerol solution applied as secondary coolant. Brazil: Associacao Brasileira de Engenharia e Ciencias Mecanicas (ABCM), Rio de Janeiro, RJ (Brazil); 2010.
[21] Shi YJ, Minami I, Grahn M, Bjorling M, Larsson R. Boundary and elastohydrodynamic lubrication studies of glycerol aqueous solutions as green lubricants. Tribology International. 2014;69:39-45.
[22] Hua J, Bjorling M, Larsson R, Shi YJ. Controllable superlubricity achieved with mixtures of green ionic liquid and glycerol aqueous solution via humidity. Journal of Molecular Liquids. 2022;345.
[23] Acuna A, Velazquez N, Sauceda D, Rosales P, Suastegui A, Ortiz A. Influence of a compound parabolic concentrator in the performance of a solar diffusion absorption cooling system. Applied Thermal Engineering. 2016;102:1374-83.
[24] Vergne P. Super Low Traction under EHD & Mixed Lubrication Regimes. In: Erdemir A, Martin J-M, editors. Superlubricity. Amsterdam: Elsevier Science B.V.; 2007. p. 427-43.
[25] Kano M, Yasuda Y, Okamoto Y, Mabuchi Y, Hamada T, Ueno T, et al. Ultralow friction of DLC in presence of glycerol mono-oleate (GMO). Tribology Letters. 2005;18:245-51.
[26] Habchi W, Matta C, Joly-Pottuz L, De Barros MI, Martin JM, Vergne P. Full Film, Boundary Lubrication and Tribochemistry in Steel Circular Contacts Lubricated with Glycerol. Tribology Letters. 2011;42:351-8.
[27] Martin JM, Donnet C, Lemogne T, Epicier T. Superlubricity of Molybdenum-Disulfide. Physical Review B. 1993;48:10583-6.
[28] Liu Z, Yang JR, Grey F, Liu JZ, Liu YL, Wang YB, et al. Observation of Microscale Superlubricity in Graphite. Physical Review Letters. 2012;108.
[29] Berman D, Deshmukh SA, Sankaranarayanan SKRS, Erdemir A, Sumant AV. Macroscale superlubricity enabled by graphene nanoscroll formation. Science. 2015;348:1118-22.
[30] Wang W, Xie GX, Lueir JB. Superlubricity of Black Phosphorus as Lubricant Additive. Acs Applied Materials & Interfaces. 2018;10:43203-10.
[31] Klein J. Hydration lubrication. Friction. 2013;1:1-23.
[32] Deng MM, Zhang CH, Li JJ, Ma LR, Luo JB. Hydrodynamic effect on the superlubricity of phosphoric acid between ceramic and sapphire. Friction. 2014;2:173-81.
[33] Deng M, Li J, Zhang C, Ren J, Zhou N, Luo J. Investigation of running-in process in water-based lubrication aimed at achieving super-low friction. Tribology International. 2016;102:257-64.
[34] Fang YF, Ma LR, Luo JB. Modelling for water-based liquid lubrication with ultra-low friction coefficient in rough surface point contact. Tribology International. 2020;141.
[35] Patir N, Cheng HS. An average flow model for determining effects of three-dimensional roughness on partial hydrodynamic lubrication. Journal of Lubrication Technology-Transactions of the Asme. 1978;100:12-7.
[36] Patir N, Cheng HS. Application of average flow model to lubrication between rough sliding surfaces. Journal of Lubrication Technology-Transactions of the Asme. 1979;101:220-30.
[37] Kogut L, Etsion I. Elastic-plastic contact analysis of a sphere and a rigid flat. Journal of Applied Mechanics-Transactions of the Asme. 2002;69:657-62.
[38] Kogut L, Etsion I. A finite element based elastic-plastic model for the contact of rough surfaces. Tribology Transactions. 2003;46:383-90.
[39] Kogut L, Etsion I. A static friction model for elastic-plastic contacting rough surfaces. Journal of Tribology-Transactions of the Asme. 2004;126:34-40.
[40] Masjedi M, Khonsari MM. Film thickness and asperity load formulas for line-contact

elastohydrodynamic lubrication with provision for surface roughness. Journal of Tribology-Transactions of the Asme. 2012;134.
[41] Chang WR, Etsion I, Bogy DB. Static friction coefficient model for metallic rough surfaces. Journal of Tribology-Transactions of the Asme. 1988;110:57-63.
[42] Johnson KL. Contact Mechanics. 1985.
[43] Roelands CJA, Winer WO, Wright WA. Correlational aspects of the viscosity-temperature-pressure relationship of lubricating oils(Dr In dissertation at Technical University of Delft, 1966). Journal of Lubrication Technology. 1971;93:209-10.
[44] Houpert L. NEW RESULTS OF TRACTION FORCE CALCULATIONS IN ELASTOHYDRODYNAMIC CONTACTS. Journal of Tribology-Transactions of the Asme. 1985;107:241-8.
[45] Peiran Y, Shizhu W. A GENERALIZED REYNOLDS-EQUATION FOR NON-NEWTONIAN THERMAL ELASTOHYDRODYNAMIC LUBRICATION. Journal of Tribology-Transactions of the Asme. 1990;112:631-&.
[46] Qu SY, Yang PR, Guo F. Theoretical investigation on the dimple occurrence in the thermal EHL of simple sliding steel-glass circular contacts. Tribology International. 2000;33:59-65.
[47] Akbarzadeh S, Khonsari MM. Thermoelastohydrodynamic Analysis of Spur Gears with Consideration of Surface Roughness. Tribology Letters. 2008;32:129-41.